EPJ manuscript No.
(will be inserted by the editor)

FERMILAB-PUB-08-661-E-PPD

The CMS Barrel Calorimeter Response to Particle Beams from 2 to 350 GeV/c

CMS HCAL/ECAL Collaborations

S. Abdullin[28], V. Abramov[31], B. Acharya[19], N. Adam[68], M. Adams[53], P. Adzic[33], N. Akchurin[59], U. Akgun[57],
E. Albayrak[57], R. Alemany-Fernandez[25], N. Almeida[25], G. Anagnostou[12,73], D. Andelin[52], E. W. Anderson[48],
M. Anfreville[9], I. Anicin[32,33], G. Antchev[50], Z. Antunovic[6], R. Arcidiacono[23], M. W. Arenton[52], E. Auffray[34],
S. Argiro[23], A. Askew[71], O. Atramentov[71], S. Ayan[57,74], M. Arcidy[50], S. Aydin[39], T. Aziz[19], M. Baarmand[61],
K. Babich[26], S. Baccaro[22,75], D. Baden[54], S. Baffioni[10], M. N. Bakirci[39], M. Balazs[52], Sud. Banerjee[19], Sun.
Banerjee[19], R. Bard[53], D. Barge[55], V. Barnes[72], D. Barney[34], L. Barone[22], A. Bartoloni[22], C. Baty[11],
H. Bawa[16], G. Baiatian[1], D. Bandurin[60], S. Beauceron[34], K. W. Bell[45], G. Bencze[14], R. Benetta[34], M. Bercher[10],
S. Beri[16], C. Bernet[10], L. Berntzon[59], U. Berthon[10], M. Besancon[9], B. Betev[36], R. Beuselinck[46], V. Bhatnagar[16],
A. Bhatti[64], C. Biino[23], J. Blaha[11], P. Bloch[34], S. Blyth[37], A. Bodek[70], A. Bornheim[67], S. Bose[19], T. Bose[69],
J. Bourotte[10], A. M. Brett[36], R. M. Brown[45], D. Britton[46], H. Budd[70], M. Buehler[52], K. Burchesky[53], P. Busson[10],
B. Camanzi[45], T. Camporesi[34], K. Canko¸cak[41,57], K. Carrell[59], E. Carrera[71], N. Cartiglia[23], F. Cavallari[22], S. Cerci[39],
M. Cerutti[10], P. Chang[38], Y. H. Chang[37], C. Charlot[10], E. A. Chen[37], W. T. Chen[37], Z. Chen[36], S. Chendvankar[19],
R. Chipaux[9], B. C. Choudhary[17], R. K. Choudhury[18], Y. Chung[70], W. Clarida[57], D. J. A. Cockerill[45], C. Combaret[11],
S. Conetti[52], F. Cossutti[24], B. Cox[52], L. Cremaldi[66], P. Cushman[63], D. G. Cussans[44], I. Dafinei[22], J. Damgov[3,49],
D. R. Da Silva Di Calafiori[36], G. Daskalakis[12], G. Davatz[36], A. David[25], P. de Barbaro[70], P. Debbins[57], K. Deiters[35],
M. Dejardin[9], M. Djordjevic[33], M. Deliomeroglu[41], R. Della Negra[11], G. Della Ricca[24], D. Del Re[22], A. Demianov[30],
A. De Min[21], D. Denegri[9], P. Depasse[11], T. de Visser[34], J. Descamps[9], P. V. Deshpande[19], J. Diaz[62], M. Diemoz[22],
E. Di Marco[22], L. Dimitrov[3], G. Dissertori[36], M. Dittmar[36], L. Djambazov[36], L. Dobrzynski[10], S. Drndarevic[32,33],
J. E. Duboscq[58], S. Dugad[19], I. Dumanoglu[39], F. Duru[57], D. Dutta[18], M. Dzelalija[6], I. Efthymiopoulos[34], J. Elias[49],
A. Elliott-Peisert[34], H. El Mamouni[11], D. Elvira[49], I. Emeliantchik[2], S. Eno[54], A. Ershov[30], S. Erturk[39,76],
S. Esen[69], E. Eskut[39], I. Evangelou[13], D. L. Evans[44], B. Fabbro[9], J. L. Faure[9], J. Fay[11], A. Fenyvesi[15], F. Ferri[9],
W. Fisher[68], P. S. Flower[45], D. Franci[22], G. Franzoni[63], J. Freeman[49], K. Freudenreich[36], W. Funk[34], S. Ganjour[9],
C. Gargiulo[22], S. Gascon[11], M. Gataullin[67], V. Gaultney[62], H. Gamsizkan[40], V. Gavrilov[28], Y. Geerebaert[10],
V. Genchev[3], F. X. Gentit[9], D. Gerbaudo[68], Y. Gershtein[71], A. Ghezzi[34], M. D. Ghodgaonkar[18], J. Gilly[10],
A. Givernaud[9], S. Gleyzer[71], S. Gninenko[27], A. Go[37], B. Gobbo[24], N. Godinovic[5], N. Golubev[27], I. Golutvin[26],
P. Goncharov[31], D. Gong[63,77], P. Govoni[21], N. Grant[44], P. Gras[9], T. Grassi[54], D. Green[49], R. J. S. Greenhalgh[45],
A. Gribushin[30], B. Grinev[43], L. Guevara Riveros[10], J. P. Guillaud[8], A. Gurtu[19], A. Murat G¨uler[40], E. G¨ulmez[41],
K. G¨um¨u¸s[59], T. Haelen[70], S. Hagopian[71], V. Hagopian[71], M. Haguenauer[10], V. Halyo[68], G. Hamel de Monchenault[9],
M. Hansen[34], M. Hashemi[20], J. Hauptman[48], E. Hazen[50], H. F. Heath[44], A. Heering[63,50], A. Heister[50], B. Heltsley[58],
J. A. Hill[45], W. Hintz[36], R. Hirosky[52], P. R. Hobson[47], A. Honma[34], G. W. S. Hou[38], Y. Hsiung[38], A. Hunt[68],
M. Husejko[25], B. Ille[11], N. Ilyina[28], R. Imlay[52], D. Ingram[57], Q. Ingram[35], E. Isiksal[41,78], P. Jarry[9], C. Jarvis[54],
C. Jeong[59], C. Jessop[65], K. Johnson[71], J. Jones[68], D. Jovanovic[32,33], K. Kaadze[60], V. Kachanov[31], V. Kaftanov[28a],
S. Kailas[18], V. Kalagin[26], A. Kalinin[31], S. Kalmani[19], D. Karmgard[65], S. K. Kataria[18], M. Kaur[16], M. Kaya[41,79],
O. Kaya[41,79], A. Kayis-Topaksu[39], R. Kellogg[54], B. W. Kennedy[45], A. Khmelnikov[31], H. Kim[59], I. Kisselevich[28],
K. Kloukinas[34], O. Kodolova[30], J. Kohli[16], P. Kokkas[13], T. Kolberg[65], V. Kolossov[28], A. Korablev[31], Y. Korneev[31],
I. Kosarev[26], L. Kramer[62], N. Krasnikov[27], A. Krinitsyn[31], A. Krokhotin[28], D. Krpic[32,33], V. Kryshkin[31],
Y. Kubota[63], A. Kubrik[55], S. Kuleshov[28], A. Kumar[16], P. Kumar[18], S. Kunori[54], C. M. Kuo[37], P. Kurt[39],
P. Kyberd[47], A. Kyriakis[12], A. Laasanen[72], V. Ladygin[26], E. Laird[68], G. Landsberg[69], A. Laszlo[14], C. Lawlor[50],
D. Lazic[50], M. Lebeau[34,80], P. Lecomte[36], P. Lecoq[34], A. Ledovskoy[52], S.-W. Lee[59], G. Leshev[36], M. Lethuillier[11],
L. Levchuk[42], S. W. Lin[38], W. Lin[37], S. Linn[62], A. L. Lintern[45], V. Litvine[67], D. Litvintsev[28,49], L. Litov[4],
L. Lobolo[62], E. Locci[9], A. B. Lodge[45], E. Longo[22], D. Loukas[12], S. Los[49], V. Lubinsky[43], P. D. Luckey[36],
V. Lukanin[31], W. Lustermann[36], C. Lynch[44], Y. Ma[67,63], E. Machado[50], H. Mahlke-Krueger[58], M. Maity[19],
G. Majumder[19], M. Malberti[21], J. Malcl`es[9], D. Maletic[33], I. Mandjavidze[9], J. Mans[68,63], N. Manthos[13], Y. Maravin[60],
C. Marchica[35,36], N. Marinelli[65], A. Markou[12], C. Markou[12], D. Marlow[68], P. Markowitz[62], M. Marone[23],
G. Martinez[62], H. Mathez[11], V. Matveev[27], C. Mavrommatis[12], G. Maurelli[11], K. Mazumdar[19], P. Meridiani[34],

---

[a] deceased

J. P. Merlo[57], H. Mermerkaya[61], G. Mescheryakov[26], A. Mestvirishvili[57], V. Mikhailin[30], P. Milenovic[33,36], M. Miller[57], G. Milleret[10], P. Miné[10], A. Moeller[57], M. Mohammadi-Najafabadi[20], A. K. Mohanty[18], P. Moissenz[26], N. Mondal[19], F. Moortgat[36], V. Mossolov[2], M. Mur[9], P. Musella[25], Y. Musienko[51,27], P. Nagaraj[19], A. Nardulli[36], J. Nash[46], P. Nedelec[8], P. Negri[21], H. B. Newman[67], A. Nikitenko[28,46], E. Norbeck[57], F. Nessi-Tedaldi[36], M. M. Obertino[23,81], J. Olson[57], Y. Onel[57], G. Onengut[39], G. Organtini[22], T. Orimoto[67], C. Ozkan[40], H. Ozkurt[39], S. Ozkorucuklu[41,82], F. Ozok[57], M. Paganoni[21], P. Paganini[10], S. Paktinat[20], A. Pal[14], A. Palma[22], B. Panev[3,35], L. Pant[18], A. Papadakis[7], I. Papadakis[12], I. Papadopoulos[13], R. Paramatti[22], P. Parracho[25], N. Pastrone[23], M. Patil[19], J. R. Patterson[58], F. Pauss[36], A. Penzo[24], E. Petrakou[12], S. Petrushanko[30], A. Petrosyan[26], D. G. Phillips II[52], V. Pikalov[31], S. Piperov[3,49], P. Piroué[68], V. Podrasky[56], A. Polatoz[39], A. Pompos[72], S. Popescu[59], C. Posch[50], A. Pozdnyakov[28], F. Ptochos[7], I. Puljak[5], A. Pullia[21], T. Punz[36], J. Puzovic[32,33], W. Qian[53], S. Ragazzi[21], S. Rahatlou[22], R. M. Ralich[61], J. Rande[9], P. A. Razis[7], N. Redaelli[21], L. Reddy[19], J. Reidy[66], D. Renker[35], S. Reucroft[51], J. M. Reymond[9], P. Ribeiro[25], U. Roeser[36], E. Rogalev[26], C. Rogan[67], Y. Roh[59], J. Rohlf[50], T. Romanteau[10], F. Rondeaux[9], M. Ronquest[52], A. Ronzhin[49], A. Rosowsky[9], C. Rovelli[22], R. Ruchti[65], P. Rumerio[34,54], R. Rusack[63], S. V. Rusakov[29], M. J. Ryan[46], A. Ryazanov[31], G. Safronov[28], L. Sala[21], R. Salerno[21], D. A. Sanders[66], F. Santanastasio[22,54], C. Sanzeni[56], L. Sarycheva[30], B. Satyanarayana[19], D. Schinzel[36], I. Schmidt[57], C. Seez[46], S. Sekmen[40], S. Semenov[28], V. Senchishin[43], S. Sergeyev[49], M. Serin[40], R. Sever[40], P. Sharp[34,46], C. H. Shepherd-Themistocleous[45], C. Siamitros[47], D. Sillou[8], J. B. Singh[16], A. Singovsky[63], Y. Sirois[10], A. Sirunyan[1], J. Silva[25], P. Silva[25], A. Skuja[54], S. Sharma[19], B. Sherwood[63], J. G. Shiu[38], R. K. Shivpuri[17], P. Shukla[18], N. Shumeiko[2], V. Smirnov[26], B. J. Smith[45], V. J. Smith[44], K. Sogut[39,83], N. Sonmez[41,84], P. Sorokin[42], M. Spezziga[59], M. Sproston[45], R. Stefanovich[2], F. Stöckli[36], V. Stolin[28], K. Sudhakar[19], L. Sulak[50], H. Suter[36], I. Suzuki[49], J. Swain[51], T. Tabarelli de Fatis[21], V. Talov[31], M. Takahashi[46], A. Tcheremoukhine[26], O. Teller[34], K. Teplov[30], K. Theofilatos[12], C. Thiebaux[10], R. Thomas[59], V. Timciuc[67], C. Timlin[46], M. Titov[9], A. Tobias[52], S. Tonwar[19], H. Topakli[39], A. Topkar[18], F. A. Triantis[13], S. Troshin[31], C. Tully[68], L. Turchanovich[31], N. Tyurin[31], K. Ueno[38], A. Ulyanov[28], A. Uzunian[31], A. Vanini[69], I. Vankov[3], I. Vardanyan[30], F. Varela[50], J. Varela[34,25], A. Vasil'ev[30], M. Velasco[55], M. Vergili[39], P. Verma[19], P. Verrecchia[9], G. Vesztergombi[14], J. Veverka[67], P. Vichoudis[34], R. Vidal[49], T. Virdee[34,46], A. Vishnevskiy[26], E. Vlassov[34,28], I. Vodopiyanov[61], I. Volobouev[59], A. Volkov[31], A. Volodko[26], H. P. Von Gunten[36], L. Wang[54], M. Wang[38], D. Wardrope[46], M. Weber[36], J. Weng[36], J. Werner[68], M. Wetstein[54], D. Winn[56], R. Wigmans[59], J. H. Williams[45], J. Whitmore[49], S. Won[55], S. X. Wu[50], Y. Yang[67], I. Yaselli[47], E. Yazgan[59], T. Yetkin[57], R. Yohay[52], A. Zabi[10], P. Zalan[14], N. Zamiatin[26], A. Zarubin[26], S. Zelepoukine[31,36], M. Zeyrek[40], J. Zhang[63], L. Y. Zhang[67], K. Zhu[67], and R. Y. Zhu[67]

[1] Yerevan Physics Institute, Yerevan, Armenia
[2] NCPHEP, Minsk, Belarus
[3] Institute for Nuclear Research and Nuclear Energy, Bulgarian Academy of Science, Sofia, Bulgaria
[4] Sofia University, Sofia, Bulgaria
[5] Technical University of Split, Split, Croatia
[6] University of Split, Split, Croatia
[7] University of Cyprus, Nicosia, Cyprus
[8] Laboratoire d'Annecy-le-Vieux de Physique des Particules, IN2P3-CNRS, Annecy-le-Vieux, France
[9] DSM/DAPNIA, CEA/Saclay, Gif-sur-Yvette, France
[10] Laboratoire Leprince-Ringuet, Ecole Polytechnique, IN2P3-CNRS, Palaiseau, France
[11] Institut de Physique Nucléaire de Lyon, Université Lyon 1, CNRS/IN2P3, Villeurbanne, France
[12] Institute of Nuclear Physics "Demokritos", Aghia Paraskevi, Greece
[13] University of Ioánnina, Ioánnina, Greece
[14] KFKI-RMKI, Research Institute for Particle and Nuclear Physics, Budapest, Hungary
[15] ATOMKI, Debrecen, Hungary
[16] Panjab University, Chandigarh, India
[17] University of Delhi, Delhi, India
[18] Bhabha Atomic Research Centre, Mumbai, India
[19] Tata Institute of Fundamental Research, Mumbai, India
[20] Institute for Studies in Theoretical Physics and Sharif University of Technology, Tehran, Iran
[21] Istituto Nazionale di Fisica Nucleare e Universita Degli Studi Milano Bicocca, Milano, Italy
[22] Università di Roma I e Sezione dell' INFN, Roma, Italy
[23] Università di Torino e Sezione dell' INFN, Torino, Italy
[24] Università di Trieste e Sezione dell' INFN, Trieste, Italy
[25] Laboratório de Instrumentação e Física Experimental de Partículas, Lisboa, Portugal
[26] JINR, Dubna, Russia
[27] Institute for Nuclear Research, Moscow, Russia
[28] ITEP, Moscow, Russia
[29] Lebedev Physical Institute, Moscow, Russia
[30] Moscow State University, Moscow, Russia

[31] IHEP, Protvino, Russia
[32] University of Belgrade, Belgrade, Serbia
[33] Vinca Institute of Nuclear Sciences, Belgrade, Serbia
[34] CERN, European Organisation for Nuclear Research, Geneva, Switzerland
[35] Paul Scherrer Institut, Villigen, Switzerland
[36] Institute for Particle Physics, ETH Zurich, Zurich, Switzerland
[37] National Central University, Chung-Li, Taiwan
[38] National Taiwan University (NTU), Taipei, Taiwan
[39] Çukurova University, Adana, Turkey
[40] Middle East Technical University, Ankara, Turkey
[41] Boğaziçi University, Istanbul, Turkey
[42] KIPT, Kharkov, Ukraine
[43] Single Crystal Institute, Kharkov, Ukraine
[44] University of Bristol, Bristol, United Kingdom
[45] Rutherford Appleton Laboratory, Didcot, United Kingdom
[46] Imperial College, University of London, London, United Kingdom
[47] Brunel University, Uxbridge, United Kingdom
[48] Iowa State University, Ames, IA, USA
[49] Fermi National Accelerator Laboratory, Batavia, IL, USA
[50] Boston University, Boston, MA, USA
[51] Northeastern University, Boston, Massachusetts, USA
[52] University of Virginia, Charlottesville, Virginia, USA
[53] University of Illinois at Chicago, Chicago, IL, USA
[54] University of Maryland, College Park, MD, USA
[55] Northwestern University, Evanston, IL, USA
[56] Fairfield University, Fairfield, CT, USA
[57] University of Iowa, Iowa City, IA, USA
[58] Cornell University, Ithaca, New York, USA
[59] Texas Tech University, Lubbock, TX, USA
[60] Kansas State University, Manhattan, Kansas, USA
[61] Florida Institute of Technology, Melbourne, FL, USA
[62] Florida International University, Miami, FL, USA
[63] University of Minnesota, Minneapolis, MN, USA
[64] Rockefeller University, New York, NY, USA
[65] University of Notre Dame, Notre Dame, IN, USA
[66] University of Mississippi, Oxford, MS, USA
[67] California Institute of Technology, Pasadena, California, USA
[68] Princeton University, Princeton, NJ, USA
[69] Brown University, Providence, RI, USA
[70] University of Rochester, Rochester, NY, USA
[71] Florida State University, Tallahassee, FL, USA
[72] Purdue University, West Lafayette, IN, USA
[73] Now at: RWTH, I. Physikalisches Institut, Aachen, Germany
[74] Now at: University of Pennsylvania, Philladelphia, PA, USA
[75] Now at: ENEA, Casaccia Research Center, S. Maria di Galeria, Italy
[76] At: Niğde University, Niğde, Turkey
[77] Now at: Southern Methodist University, Dallas, TX, USA
[78] At: Marmara University, Istanbul, Turkey
[79] At: Kafkas University, Kars, Turkey
[80] Now at: University of Athens, Greece
[81] Now at: Università del Piemonte Orientale, Novara, Italy
[82] At: Süleyman Demirel University, Isparta, Turkey
[83] At: Mersin University, Mersin, Turkey
[84] At: Izmir Yüksek Teknoloji Enstitüsü, Izmir, Turkey

Received: date / Revised version: date

Abstract. The response of the CMS barrel calorimeter (electromagnetic plus hadronic) to hadrons, electrons and muons over a wide momentum range from 2 to 350 GeV/c has been measured. To our knowledge, this is the widest range of momenta in which any calorimeter system has been studied. These tests, carried out at the H2 beam-line at CERN, provide a wealth of information, especially at low energies. The analysis of the differences in calorimeter response to charged pions, kaons, protons and antiprotons and a detailed discussion of the underlying phenomena are presented. We also show techniques that apply corrections to the signals from the considerably different electromagnetic (EB) and hadronic (HB) barrel calorimeters in reconstructing the energies of hadrons. Above 5 GeV/*c*, these corrections improve the energy resolution of the combined system where the stochastic term equals 84.7±1.6% and the constant term is 7.4±0.8%. The corrected mean response remains constant within 1.3% *rms*.

Correspondence to: Nural.Akchurin@ttu.edu

1 Introduction

The CMS calorimeters have distinct hadronic (HCAL) and electromagnetic (ECAL) systems. The central HCAL is made of brass and scintillators [1] while the ECAL comprises lead tungstate crystals ($\mathrm{PbWO_4}$) [2]. The calorimeters are divided into the barrel (HB and EB) and the end-cap (HE, EE and pre-shower, ES) sections inside a cryostat of 5.9 m inner diameter, containing a superconducting solenoidal coil providing a 4-T magnetic field. The HB design maximizes the number of interaction lengths (λ_{I}) inside the cryostat and is limited to $5.8\lambda_{\mathrm{I}}$ at $\eta = 0$. The EB adds 1.1 λ_{I} and the material between EB and HB adds another 0.1 λ_{I}. The outer hadron calorimeter (HO) was constructed to sample the energy leakage outside of the cryostat [3]. There are also two forward calorimeters (HF) made of iron and quartz fibers [4]. Figure 1 shows a schematic of the calorimeters inside and around the magnet.

This paper reports on the barrel calorimeter (HB, HO and EB) responses to beam particles. The measurements were performed with production modules and front-end electronics as in the final CMS detector configuration. A special beam line was constructed to measure the calorimeter response down to 2 GeV/c. This was necessary since a large fraction of the particles reaching the CMS calorimeters in the LHC will have energies below 20 GeV.

1.1 HCAL Barrel (HB) Calorimeter

The HB and HO are designed to measure the timing, angular direction and energy of hadronic showers. These quantities are needed for the calorimetric triggers and online reconstruction of jets and missing transverse energy. The cylindrically symmetric HB surrounds the EB. It consists of alternating layers of brass and plastic scintillator tiles (3.7 mm SCSN81 from Kuraray except the innermost layer 1.0 cm BC408 from Bicron). The HB design necessarily requires minimizing the amount of space devoted to the active medium. The scintillator tiles are read out with embedded wavelength shifting (WLS) fibers. Brass was chosen as the absorber material because it is non-magnetic and cost is affordable. This design makes construction relatively simple, lends itself to projective tower geometry, and eliminates uninstrumented gaps. The brass type is C26000 (cartridge brass) and is composed of 70% Cu and 30% Zn. The brass density is 8.83 g/cm^3 with interaction length $\lambda_{\mathrm{I}} = 16.4$ cm and radiation length $X_0 = 1.5$ cm.

The HB covers the pseudorapidity range $|\eta| < 1.3$ and consists of 36 identical azimuthal wedges ($\Delta\phi = 20^\circ$) which form two half-barrels (HB+ and HB-). Each half-barrel is inserted from either end of the cryostat and positioned around the central axis of the CMS magnet. Each wedge is further segmented into four azimuthal ($\Delta\phi = 5^\circ$) sectors. The plates are bolted together in a staggered geometry resulting in a configuration that contains no projective passive material for the full radial extent of a wedge. The innermost and outermost plates are made of stainless steel to provide structural strength. The scintillator is divided into 16 η sectors, resulting in a tower segmentation of $(\Delta\eta, \Delta\phi) = (0.087, 0.087)$.

Each wedge contains 72 channels of front-end electronics mounted on the detector periphery near $|\eta| \approx 1.3$. These circuits are housed in an enclosure referred to as a readout box (RBX). Each of these RBXs is further divided into four readout modules (RM). A single RM contains a 19-channel hybrid photodiode (HPD) that registers signals from 16 η towers of a single ϕ sector.

The HPD is a planar structure consisting of a photocathode and a silicon diode separated by 3.5 mm of vacuum. Photoelectrons are accelerated by a ~8-kV potential and strike the diode causing ionization which results in a gain of 1,600. The diode consists of 19 electrically independent readouts. The HPD signals are fed into three 6-channel readout cards located inside the RM, based on a custom ASIC which performs charge integration and encoding (QIE). The *rms* noise per tower is about 200 MeV. For the HB, six time samples (6×25 ns) from 3×3 HB towers were used for energy reconstruction. The signal is about 75 ns wide with a small tail extending another 50 ns. The zero input response of the QIE (pedestals) are measured and subtracted for each run.

The QIE is a non-linear multi-range ADC designed to provide approximately constant fractional precision over a wide dynamic range. This is accomplished with a floating-point analog-to-digital conversion in which the bin width in each of four ranges is increased in proportion to the input amplitude. In addition, the QIE has four time interleaved stages. The output of the QIE contains 2 bits of range (exponent) and 5 bits of mantissa. Details of the HB geometry, construction and electronics are reported elsewhere [5–8].

The design of the outer calorimeter (HO) scintillating tiles is similar to that of the HB. The scintillator plates are 1 cm thick BC408. The HO counters are grouped in six segments and the transverse segmentation is identical to that of the HB. Two layers of scintillating tiles are inserted in the central muon system while the other two rings have one layer of scintillating tiles (see Figure 1). The readout and the electronics for HO are the same as in the HB system.

1.2 ECAL Barrel (EB) Calorimeter

The electromagnetic calorimeter used for these measurements consisted of a complete production EB Supermodule (SM) of width $\Delta\phi = 20^\circ$ containing 1,700 crystals. The EB crystals are slightly tapered with front-face dimensions of 2.2×2.2 cm^2 and a crystal length of 23 cm or $25.8X_0$ (see Section 4.3 for discussion on the interaction length). In order to avoid cracks in the barrel, the axes of the crystals are tilted by 3° in both polar and azimuthal angle with respect to the direction of particle tracks originating from the interaction point. The EB covers a range $|\eta| < 1.48$ and consists of 36 SMs containing 61,200 crystals.

The light emitted in the crystals is converted to an electrical signal using avalanche photodiodes (APD). Two APDs (Hamamatsu S8148) are glued to the back of each crystal. The *rms* electronics noise per crystal was found to be about 45 MeV. A minimum ionizing particle deposits about 250 MeV over the full length of the crystal [9,10].

The EB signal from the APD is amplified and shaped before being digitized by the ADC clocked at 40 MHz. The energy in the EB is computed as a weighted sum of several time samples of the waveform. The choice of weights and the number of samples are dictated by the desire to minimize the noise which is measured with no input signal (pedestal). In the test beam environment, the phase with respect to the 40 MHz clock is random. Even though the signal is about 200 ns wide, only six time samples (6×25 ns) from 7×7 crystals were used for energy reconstruction with pedestal subtraction.

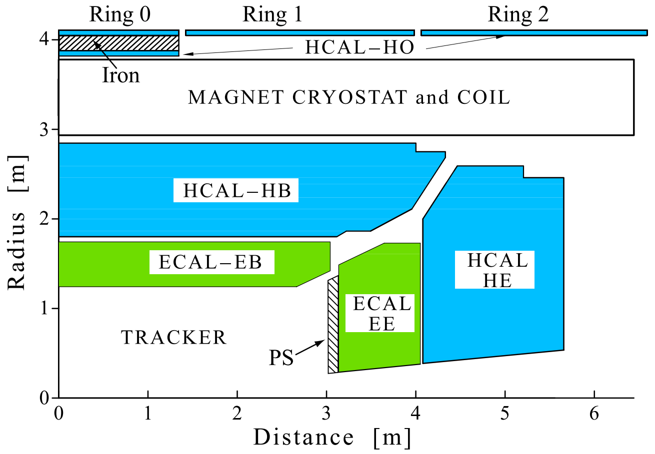

Fig. 1. Location of the ECAL and the HCAL detectors (quarter slice-longitudinal cross section) in and around the CMS magnet.

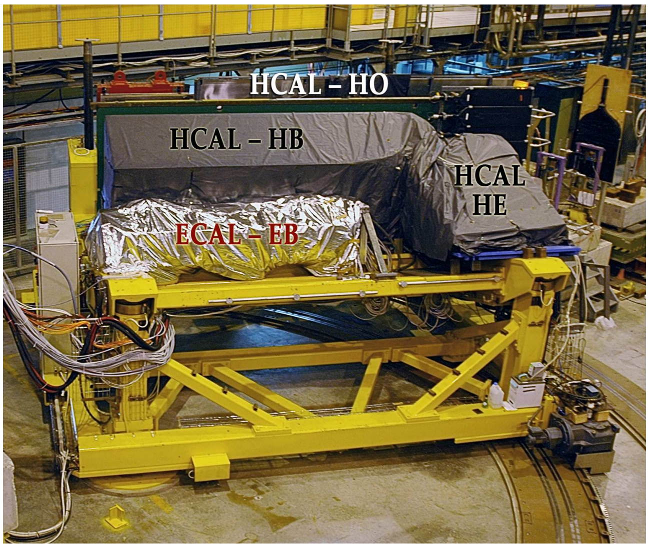

Fig. 2. The ECAL and the HCAL modules on a moving platform in the CERN H2 test beam area. The transporter table which supported the wedges is designed to move in ϕ and η directions, approximately 0 to 30° in ϕ and 0 to 3.0 in η.

2 Test Beam Setup

The data were recorded during 2006 at the CERN H2 test beam. Figure 2 shows a photograph of the moving platform that held two production HB wedges plus a production EB SM which was placed in front of the HB, and the HO behind the HB. The HE module seen on the platform was not used in this test. The placement of the components is in the same geometric relationship as in the CMS experiment. The two-dimensional movement of the platform in the ϕ and η directions allowed the beam to be directed onto any tower of the calorimeter mimicking a particle trajectory from the interaction point of the CMS experiment. Four scintillation counters were located three meters upstream of the calorimeters and a coincidence between a subset of the counters was used as the trigger.

Temperature stability is critical for the ECAL as both the response of the crystals and the APDs change with temperature. The temperature was stabilized by enclosing the EB SM (except in the beam direction) in 5 cm aluminum plates with cooling water pipes embedded in the plates. The entire SM was wrapped with a thermal blanket and the temperature was stabilized at 21°C within ±0.05°C.

2.1 H2 Beam Line and Particle Identification

Because a tertiary beam was required to study low momentum (< 10 GeV/c) particles, considerable effort was made to clean up the beams and perform particle identification. Figure 3 schematically depicts the CERN H2 beam line. The beam line is designed to operate in two distinct modes. In the high energy mode, various particles are produced when 450 GeV/c protons from the Super Proton Synchrotron (SPS) strike a production target (T2) 590.9 m upstream of the calorimeters, and particle momenta range between 15 GeV/c and 350 GeV/c. In the very low energy (VLE) mode, an additional target (T22) located 97.0 m upstream of the calorimeter is used for particle production and the momenta of particles are limited to ≤ 9 GeV/c. As shown in Figure 3, a dog-leg configuration is utilized for the momentum selection of these low momentum particles.

In the high energy mode, the T22 target and the VLE beam dump were removed from the beam line. The maximum usable beam momentum was 100 GeV/c for electrons and 350 GeV/c for hadrons. In the VLE mode, two Cherenkov counters (CK2 and CK3), two time-of-flight counters (TOF1 and TOF2) and muon counters (Muon Veto Wall (MVW) of 100×240 cm^2, Muon Veto Front (MVF) of 80×80 cm^2 and Muon Veto Back (MVB) of 80×80 cm^2) were used to positively tag electrons, pions, kaons, protons, antiprotons and muons.

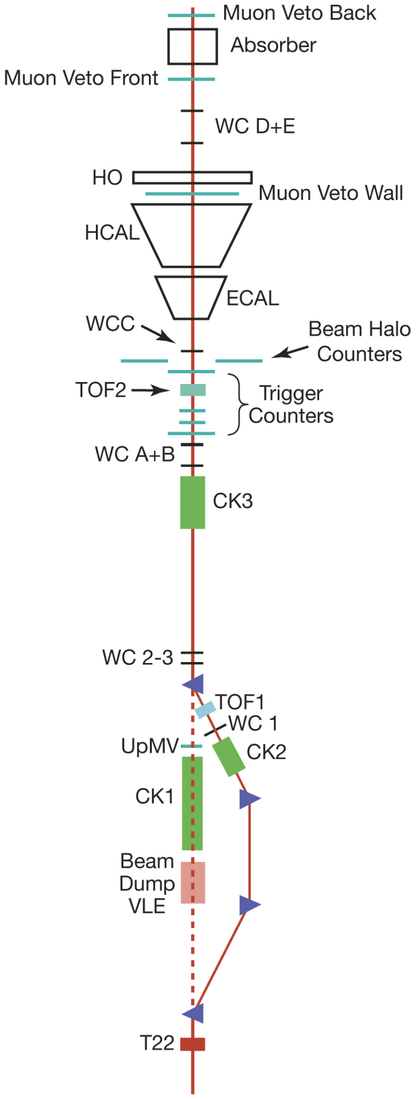

Fig. 3. The CERN H2 beam line and the experimental setup are shown schematically. In the VLE mode, the T22 target and a beam dump were inserted into the beam line, and the low energy particles were steered through the dog-leg.

CK2 is a 1.85-m long Cherenkov counter filled with CO_2 and was used to identify electrons in the VLE mode. At 0.35 bar, no other charged particles gave a signal and the counter was better than 99% efficient in identifying electrons. It produces 6 photoelectrons (*pe*) for particle passage with $\beta = 1$. CK3 is also 1.85-m long and was filled with Freon134a [11]. The pressure in CK3 was set depending on the desired discrimination between electrons, pions, and kaons. For example, at lower beam momenta, ($P_b \leq 3$ GeV/c), it was set to tag electrons at 0.88 bar yielding 19 *pe* for $\beta = 1$. At higher momenta ($P_b > 4$ GeV/c), CK3 was usually run at 1.2 bar in order to separate pions from kaons and protons where a $\beta = 1$ particle yielded 25.5 *pe*.

Time-of-flight counters (TOF1 and TOF2) were separated by ~55 m. Each scintillator plate was 10×10 cm^2 in area and 2-cm thick. Two trapezoidal air-core light guides on either side of the plate funneled the scintillation light to two fast photomultiplier tubes (Hamamatsu R5900). The analog pulses were discriminated by constant fraction discriminators. The time resolution obtained by this system was ~300 ps. Protons were well-separated from pions (and kaons) up to 7 GeV/c with this time-of-flight system alone. Pions and kaons have $\pm 1\sigma$ TOF overlap at momenta of 5.6 GeV/c, while kaons and protons overlap at 9.5 GeV/c. Figures 4 and 5 display the identified particles in 3 and 8 GeV/c negative hadron beams.

Energetic muons were tagged with MVF and MVB counters as well as the MVW counters. MVF and MVB were large (80×80 cm^2) scintillation counters and were placed well behind the calorimeters. In order to absorb the soft muon component in the beam line, an 80-cm thick iron block was inserted in front of MVB. When tested with a pure muon beam at 225 GeV/c, the efficiency of muon rejection was found to be better than 99%. MVW consisted of 8 individual scintillation counters, each measuring 80×100 cm^2, placed closely behind the HB. These counters were positioned horizontally with a 2-cm overlap between them, hence covering a region of 226 cm in the vertical and 100 cm in the horizontal directions. In addition to tagging low momentum (2-5 GeV/c) beam muons, MVW was also used to study the details of late developing hadronic showers.

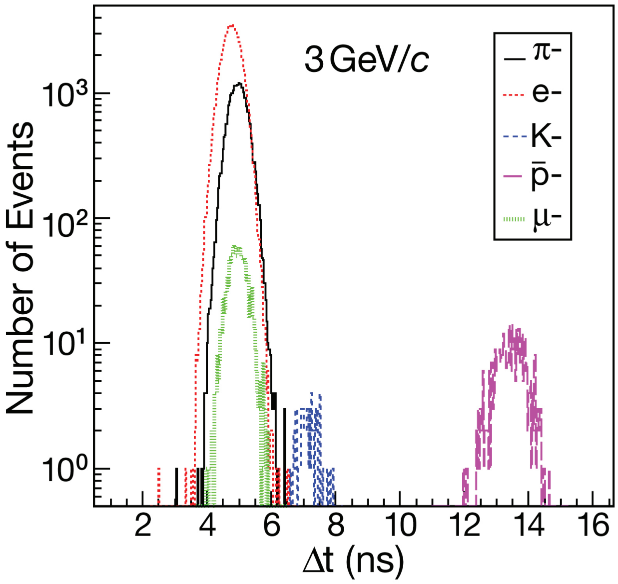

Fig. 4. The particle identification was carried out with CK2 and CK3, TOF1 and TOF2, and MVW in the VLE mode. The distributions of the time of flight between TOF1 and TOF2 are shown for different particles.

In addition to the aforementioned particle ID detectors, six delay-line chambers (WC1 through WC3 and WCA through WCC upstream of the EB+HB), four scintillation counters (S1 through S4) for triggering and four scintillation beam halo counters (BH1 through BH4) were

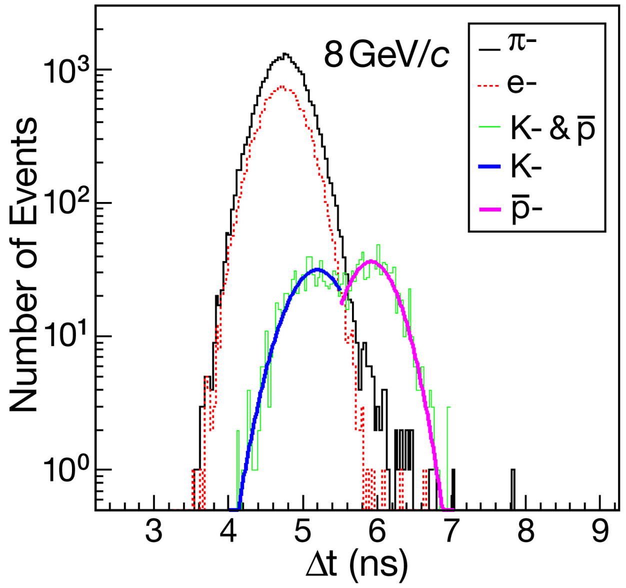

Fig. 5. The same as Figure 4 but for an 8 GeV/c negative hadron beam. The solid blue and purple lines indicate fits to data (green histogram) for K^- and $\bar{p}$, respectively.

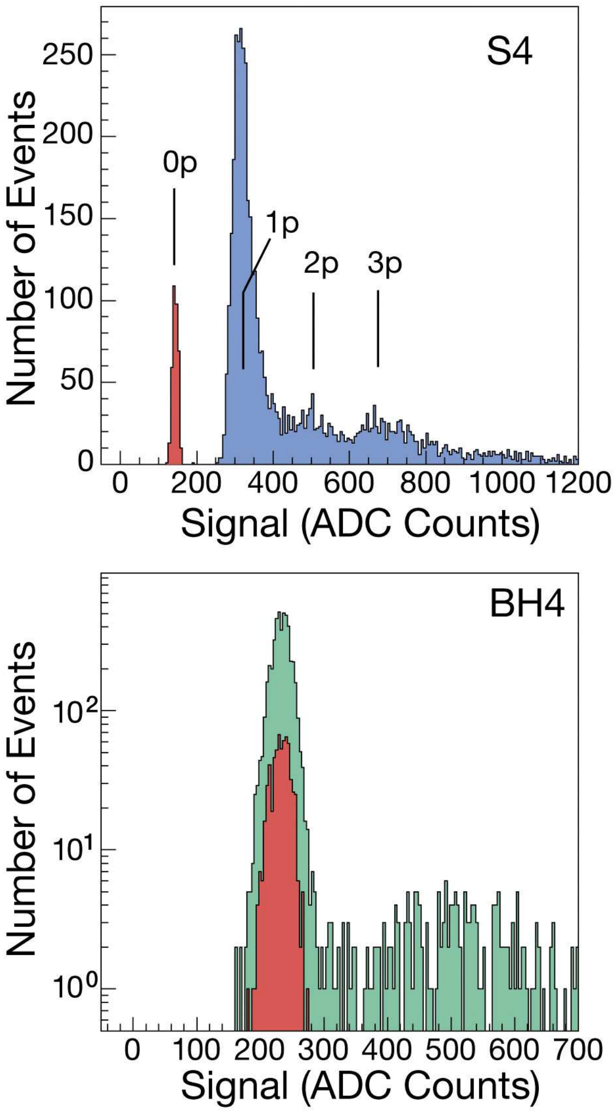

Fig. 6. The signal distribution from the S4 trigger scintillator (top) for 50 GeV/c electrons displays multi-particle events where up to three particles are clearly discernible. The bottom plot shows the signal distribution of one of the four halo counters for 3 GeV/c negative pion beam. The red histograms indicate pedestal distributions.

used in the experiment. The spatial resolution afforded by the delay-line chambers was ∼350 μm in both the x- and y-coordinates. The beam trigger typically consisted of the coincidence S1·S2·S4 which defined a 4×4 cm^2 area on the front face of the calorimeter. The S4 counter pulse height was used to eliminate multi-particle events off-line since it gave a clean pulse height distribution for single and multiple particles in the beam (see Figure 6). BH counters, each measuring 30×100 cm^2 in size, were arranged such that the beam passed through a 7×7 cm^2 opening. These counters were positioned 17 cm downstream of the last trigger scintillator S4 and were effective in vetoing the beam halo and large-angle particles that originated from interactions in the beam line.

2.2 Beam Composition

In the high energy mode of the beam line, data were generally taken with negative beams. In this mode, there was no anti-proton contamination. If the beam line was configured for positive particles, at very high momenta, *e.g.* 350 GeV/c, the beam consisted almost purely of protons. At 20 and 30 GeV/c, the proton identification in the π^+ beam was readily possible when CK3 was pressurized to 1.7 bar of CO$_2$.

The particle content depends on the momentum. At the higher end, pions dominate. At lower momenta, the beam consisted mostly of electrons. The beam consisted of 31% pions, 0.4% kaons, and 5.6% protons at +4 GeV/c, and the remaining particles were positrons. At +8 GeV/c, the beam contained 72% pions, 2% kaons and 7% protons, and the remaining fraction consisted of positrons. In the negatively charged beam, the particle mixture was approximately the same but the antiproton fraction was much reduced compared to that of the proton in the positive beam.

The beam content of the very low energy (VLE) beam is shown in Table 1. The average uncertainty on the beam fractions was 0.7% for π^- and electrons, and 0.4% for π^+ and positrons below 9 GeV/c. At 9 GeV/c, these uncertainties were 7.2% and 5.2%, respectively. At beam momentum 4 GeV/c and lower, the electrons were double tagged by CK2 and CK3 with extremely high efficiency. Above 4 GeV/c, CK3 was used to separate pions from kaons and protons. In order to enrich the hadron content of beam triggers at low momenta, a S1·S2·S4·$\overline{\text{MVF}}$ trigger was employed.

The uncertainty in pion *vs* electron identification in general does not exceed 0.5% in the VLE mode. This uncertainty is larger and estimated to be 1.8% and 6% using the information from the calorimeter and Chenerkov counters at 3 and 8 GeV/c.

Table 1. The first and second numbers in each column is the fraction of the negative and positive charged particles respectively in the VLE mode.

P_b [GeV/c]	(π^-, π^+) [%]	(e^-, e^+) [%]	$(\bar{p}, p)$ [%]	(K^-, K^+) [%]
9	73.0, 68.8	22.1, 20.8	2.7, 7.6	2.3, 2.7
8	56.9, 71.8	39.8, 19.1	1.9, 7.1	1.4, 2.1
7	61.8, 67.2	35.5, 23.8	1.7, 7.2	1.0, 1.7
6	57.7, 60.6	40.1, 31.3	1.5, 6.8	0.8, 1.4
5	53.2, 51.4	44.9, 40.7	1.2, 6.6	0.7, 1.2
4	40.9, 31.3	58.0, 62.7	0.9, 5.6	0.2, 0.4
3	25.9, 21.9	73.7, 73.5	0.3, 4.5	0.1, 0.1
2	10.6, 8.5	89.3, 89.2	0.1, 2.3	0.01, 0.01

3 Calibration of Calorimeters

Both the EB and HB calibrations were carried out with 50 GeV/c electrons. The HB calibration was performed before the EB SM was mounted in front of the HB. The electron beam was directed at the center of each tower. Similarly, the EB calibration data were collected by pointing the beam to a selected set of crystals that formed a tight grid pattern. The *rms* value of the linearity between 2 and 9 GeV/c is 0.5% and less than 1% for higher energies.

The reconstructed energy was determined to be the sum of energies recorded by the EB and HB. We refer to it as the raw energy throughout this paper. For the EB, the signals from 7×7 crystals, and for the HB the signals from 3×3 towers were summed. For pion showers the 7×7 crystals contained over 99% of the energy, and the 3×3 HB towers contained over 98% of the energy. In the case of the HO, the total energy was estimated by adding signals from 3×2 towers. In each case the energy is sampled over 6 time slices (6×25 ns) and pedestals subtracted.

The response of each HB scintillator tile of each layer was also measured by using a 5-mCi Co^{60} moving wire radioactive source [12]. The signal from a tower was calculated by taking the average of all measurements from the scintillator layers and weighting these averages by the shower profile. During the construction phase, every scintillator tile was tested with a radioactive wire source. This procedure makes it possible to transfer the beam calibration constants for each tower that were not placed in the test beam. The precision of tower-to-tower calibration was measured to be 2% as derived by comparing the consistency of the relative source and the beam data measurements.

Figure 7 shows the beam calibration constants in GeV/fC for four ϕ segments as a function of η tower numbers. The combined effect of the light attenuation in the optical fibers, loss in fiber connectors and the HPD gain differences are evident in the figure. The drop of the gain with increasing η is due to the longer length of the optical fiber. The η towers in a single ϕ segment are measured by a single HPD which has the same gain for each pixel.

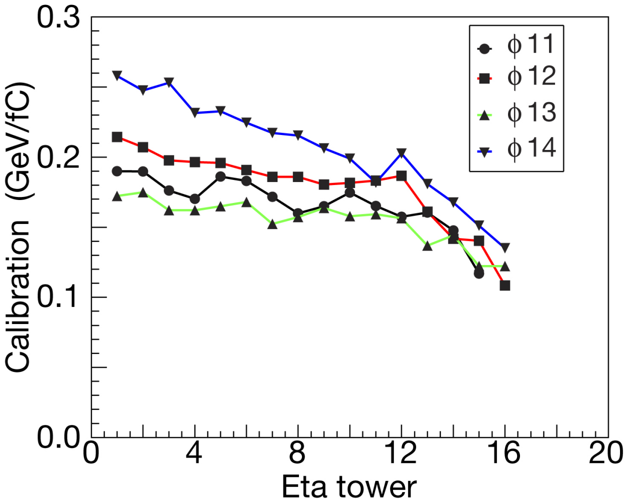

Fig. 7. Calibration constants for the 4 ϕ sectors ($\Delta\phi = 5^{\circ}$) of the HB wedge used in this beam test.

At higher beam momenta ($\geq$ 50 GeV/c) the longitudinal energy leakage behind the EB+HB is noticeable. To measure this leakage, the HO sampling layers were constructed and inserted in the barrel muon system to reduce these fluctuations. The HO layers (see Figure 1) are placed behind the CMS solenoid cryostat. The HO system is divided into six sections that follow the division of the barrel muon system. Ring 0 (+ and −) are in the central muon system and are composed of two layers of scintillators one immediately outside of the magnet cryostat and the other layer after a 15-cm thick iron layer. Ring 0 in the muon barrel system YB0 (the central part of CMS) covers the $|\eta|$ range of 0 to 0.35. Rings +1, −1, +2 and −2 are single layer scintillators inserted in the muon barrel systems YB1 and YB2 on both positive and negative sides of CMS immediately inside the first muon iron layer covering the $|\eta|$ range of 0.35 to 1.2. In the test beam setup, the HO was placed behind the HB covering 30° in ϕ and the full η range. To mimic the magnet solenoid system, an aluminum block was inserted between the HB and HO. Also inserted was a 15 cm thick iron block between scintillator layers 1 and 2 of Ring 0 similar to the CMS detector to contain the showers. Both the aluminum and iron blocks had the same geometrical size and placement as in CMS. The HO modules were first calibrated by 150 GeV/c μ^- beam. A clear μ peak beyond pedestal was observed in Ring 0 and Ring 2. In Ring 1 the μ peak was measurable but not as cleanly separated. Next, the HO energy scale was determined by 300 GeV/c π^- beam impinging on η tower 4 of the HB. For this measurement, it was also required that the energy in the EB be less than 1.2 GeV to constrain the energy sharing between the HB and HO only. The energy scale was determined by requiring the best energy resolution in HB+HO, as measured by *rms* width, for the 300 GeV/c π^- beam.

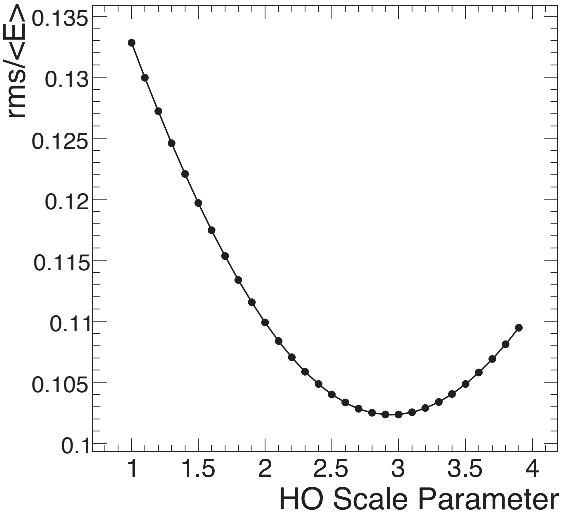

Fig. 8. The energy resolution of the HB+HO response to 300 GeV/c π^- as a function of HO scale parameter. The curve shown is a fit to the data.

Figure 8 displays the *rms* energy resolution for the HB+HO for 300 GeV/c π^- as a function of the HO energy scale parameter. The chosen scale parameter (2.9) is the one that minimizes the combined energy resolution. Comparison of the HCAL energy spectra with and without the HO is shown in Figure 9. It is clear that the fluctuation in energy leakage behind the HB+HO is reduced by the introduction of the HO.

4 Combined Calorimeter (EB+HB) Response

Figure 10 shows the combined response of the EB+HB calorimeter to a variety of particles in a wide range of momenta. We define the particle response as the average calorimeter signal per unit energy, normalized to unity for electrons. Neither noise suppression nor Gaussian fitting is used in the particle response determination. At 5 GeV/c, for example, the antiproton response is ~70% of the electron response. The responses to charged pions and protons are 62% and 47% of the electron response at the same energy, respectively. At a given momentum, the available energy that is converted to a calorimeter signal varies by particle type. The available energy for protons is their kinetic energy. For antiprotons, the available energy equals the kinetic energy plus twice the rest mass of the proton. For pions and kaons, the available energy is their kinetic energy plus their mass. In Figure 11, the same data are plotted against the available energy, *i.e.* energy that contributes to the generation of an observable signal. One expects roughly the same response characteristics for all hadrons, as observed in the data, but there are subtle differences which we discuss next.

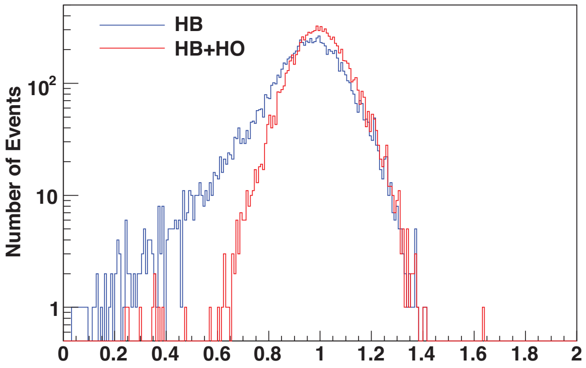

Fig. 9. The histograms are for the HB alone (blue), and for the HB+HO (red) with the optimal scale factor for the HO. The signal distributions are scaled such that 300 GeV/c is unity.

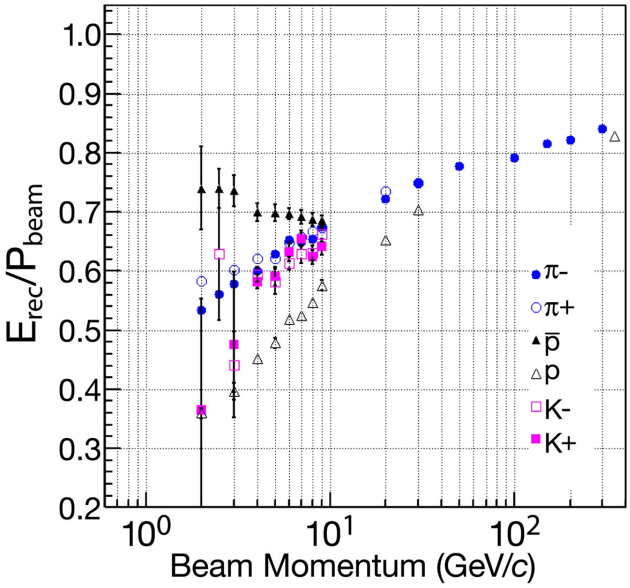

Fig. 10. The response of the combined calorimeter system to six different particles is shown as a function of the beam momentum. Both the EB and HB are calibrated with 50 GeV/c electrons.

4.1 (π^+/π^-) Response Ratio

The response to π^+ below 5 GeV/c is larger than the π^- response, increasing as the energy decreases. One possible

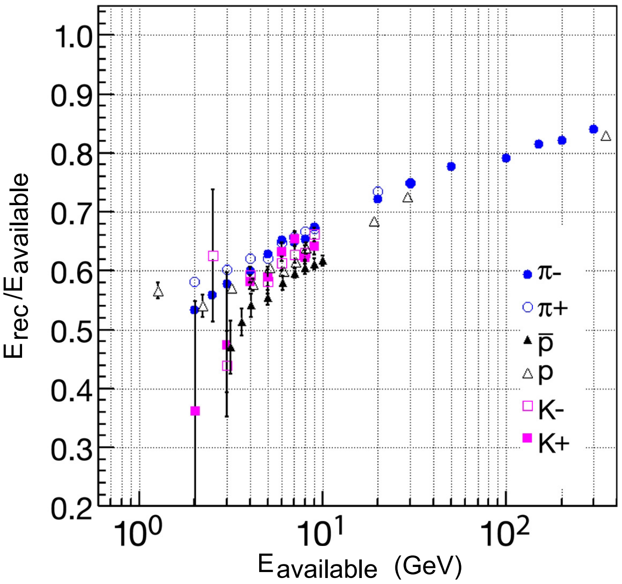

Fig. 11. The data are the same as in Figure 10 but the calorimeter response is plotted against the available energy.

interpretation of this fact is due to the characteristics of the charge exchange reactions, $\pi^+ + n \rightarrow \pi^0 + p$ (I) and $\pi^- + p \rightarrow \pi^0 + n$ (II). π^0 develops electromagnetic showers which give about 20% more signal compared to hadrons. The π^0 production is deduced to be 10% higher at 2 GeV/c for π^+ beam compared to π^- beam and by 5 GeV/c the π^0 is about 5% lower [13]. Since the target material ($PbWO_4$) consists of about 42% more neutrons than protons, the relative effect of reaction (I) is larger than that of reaction (II). Figure 12 shows this effect to be about 10% at 2 GeV/c.

4.2 (π/p) Response Ratio

The response to protons is systematically lower than that of negative or positive pions. The most likely interpretation of this effect, also observed at high energy, is a result of the fact that π^0 production is, on average, smaller in proton induced showers. This is a consequence of baryon number conservation, which favors the production of leading baryons, while pion induced reactions may have leading π^0s. This effect was clearly observed in the HF calorimeter [14], where it caused a response difference in excess of 10%. Since the e/h values of the EB+HB are smaller than for the HF [15], the effects are correspondingly smaller but nevertheless significant.

4.3 (π/p) Response Ratio in EB

Since the inelastic cross sections for protons is larger than for pions, a larger fraction of the baryons start showering in the EB. This is illustrated in Figure 13, which shows that 41% of the pions penetrate the EB without starting a shower, versus 35% for protons. The effective thickness of the EB is thus $1.05\lambda_I$ for protons and $0.89\lambda_I$ for pions.

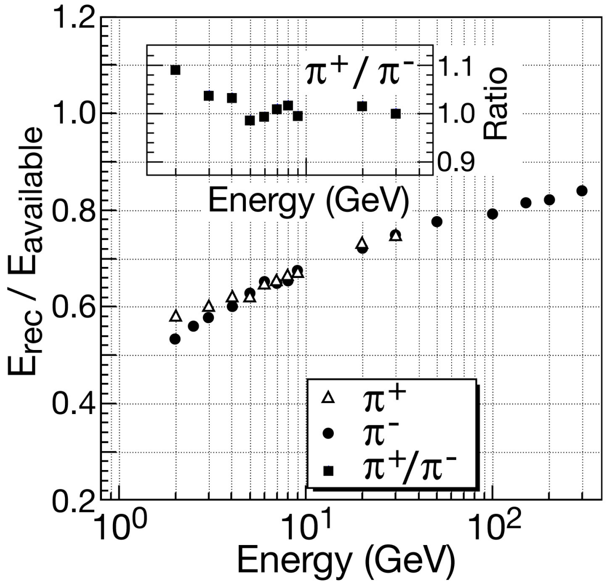

Fig. 12. The calorimeter response of π^+ and π^-. The black squares represent the response ratio between π^+ and π^-. Statistical errors are smaller than the symbol size.

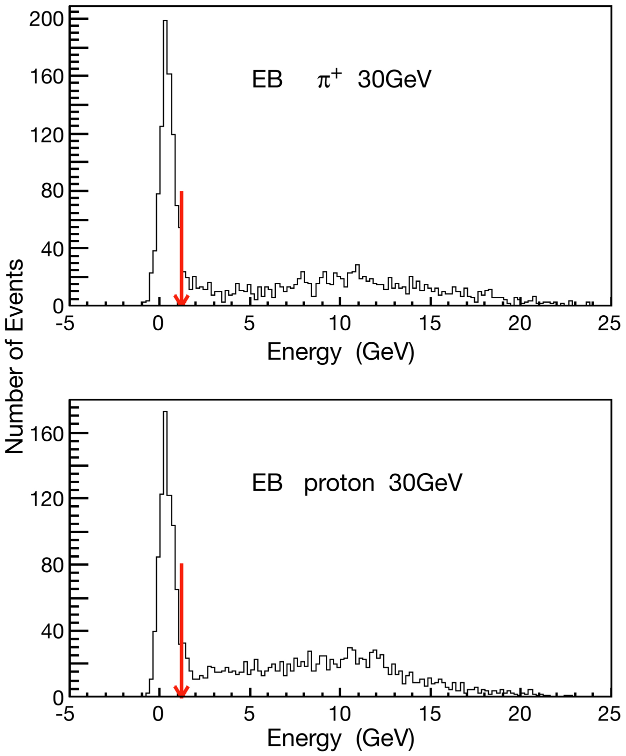

Fig. 13. The signal distributions for 30 GeV/c pions (top) and protons (bottom) for the same number of events in the EB are shown. The arrow indicates where the cut is applied (1.2 GeV) to separate non-interacting pions and protons from the interacting ones.

Figure 14 shows the EB energy spectra for 300 GeV/c negative pions and 350 GeV/c protons. At 350 GeV/c the positive beam is exclusively protons. The highest momentum for negative beam with sufficient intensity is about 300 GeV/c. The ratio of non-interacting particles (proton/pion) in EB is ~1.2 consistent with the ratio of λ_I. In addition for pions that interact in EB the energy in EB is larger due to the greater fraction of π^0 production versus that of protons.

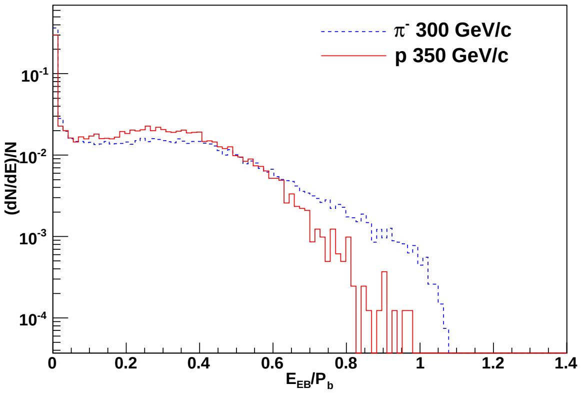

Fig. 14. The EB energy distribution for 300 GeV/c pions and 350 GeV/c protons. The two histograms contain the same number of entries and the horizontal axis is normalized by the beam momentum.

4.4 Comparison of π, p and $\bar{p}$ Response

The fraction of the beam energy deposited in the EB decreases from ~60% at 2 GeV/c to ~25% at 300 GeV/c. At the same incident momentum, protons deposit on average less energy than pions in the EB, while antiprotons deposit more than pions. Antiprotons start their showers, on average, earlier than pions and therefore a larger fraction of the energy ends up in the EB. At first sight, one would expect the same for proton induced showers. However, when a proton interacts in the EB, the interactions have limited energy transfered to secondary π^0s because the final state should contain two baryons. This effect suppresses the proton signal in the EB, despite the fact that protons are more likely to start their showers in the EB compared to pions. The requirements of baryon number conservation do not limit π^0 production for antiproton induced showers. In first approximation, there is no difference with pion induced showers. Therefore, the EB/HB energy sharing properly reflects the difference in interaction length in this case.

The effects mentioned above also explain why the antiproton response is systematically smaller that the pion response (Figure 10). Antiprotons are more likely to start showering in the EB compared to the pions. Pions deposit, on average a larger fraction of their energy in the HB. And since the e/h value of the HB is smaller than for the EB, the pions benefit more from the increased response to the non-electronmagnetic shower components.

4.5 μ Response

Figure 15 shows the response of 150 GeV/c muons in the HB using 3×3 HB tower structure. Even though 9 towers were read, only the central tower has a signal above pedestal. Since the noise in a single tower of the HB is equivalent to ~0.2 GeV, this calorimeter system is superb in identifying single isolated muons. The HB trigger electronics is also designed to generate an isolated muon signal (bit) based on this capability. Muons can also be used as a relative calibration of every tower. Using the 50 GeV/c electron calibration, the mean energy deposited by a 150 GeV/c muon is 2.4 ± 0.1 GeV. If the pion calibration correction is applied, the mean energy deposited is at 2.8 ± 0.2 GeV.

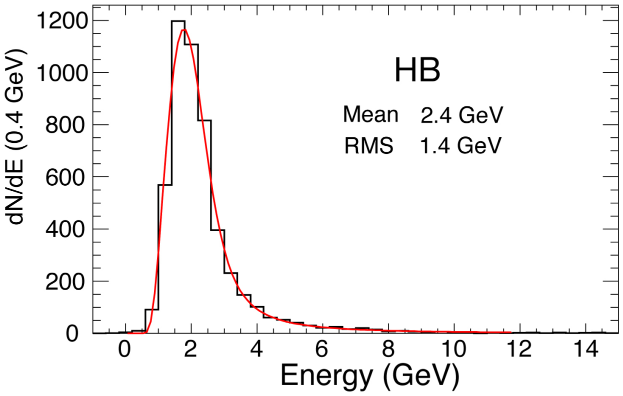

Fig. 15. The HB response to 150 GeV/c μ^- from tower 4 ($\eta = 0.3$). The solid curve represents a fit using combined Gaussian and Landau distributions.

5 Optimization of Energy Reconstruction

The total energy in the CMS central calorimeter system is the sum of signals from the EB, HB and HO. The e/h values are very different for the EB and the HB, and thus corrections have to be applied to obtain the true particle energy from the combined system.

Figure 16 displays the measured energy correlations in the EB *vs* HB towers for a number of pion beams. In a compensating calorimeter ($e/h = 1$), the events would lay about the solid lines as indicated in Figure 16. This is not the case for the EB+HB system, and thus we perform optimization of the *energy response* in three steps using the cluster energies from 7×7 EB crystals, 3×3 HB and 3×2 HO towers. We consider energies at least 3σ away from the noise level (0.8, 1.0 and 2.0 GeV for the EB, HB and HO clusters, respectively). In this section, the measured energy always refers to the *cluster energy* unless specified

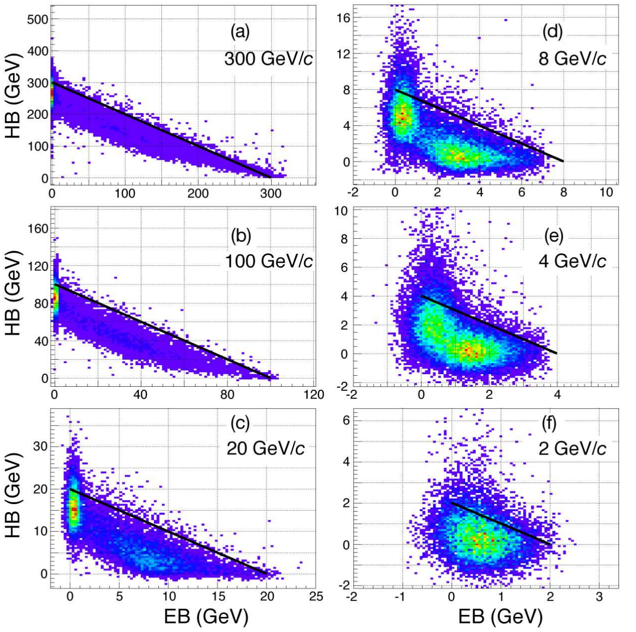

Fig. 16. The raw energy deposit correlations between the EB and HB for 300, 100, 20, 8, 4 and 2 GeV/c π^-s. The straight line indicates the behavior of a compensating calorimeter system.

otherwise. The first correction is carried out for the HB energy response using minimally ionizing events in the EB. The next step utilizes the corrected energies in the HB and the beam constraint to correct the energy measured by the EB. It is important to note that the usage of the known beam momentum at this point is only to determine the parametrization. Finally, using the corrected EB and HB energies from the above steps, the nonlinear response of the combined EB+HB system as a function of the EB energy fraction is corrected using a third order polynomial.

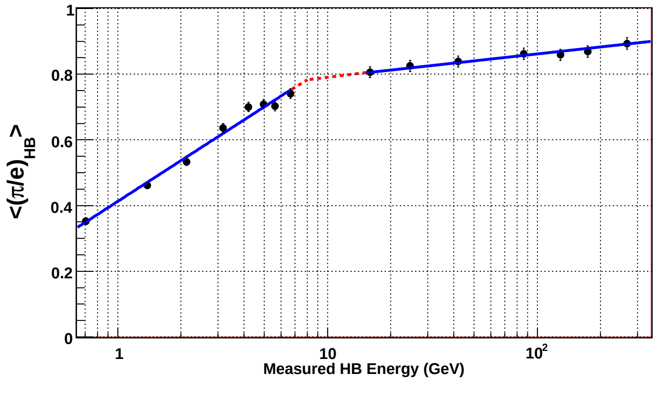

Fig. 17. π/e *vs* $E_{\rm HB}$ for events interacting in the HB. The data are fit to two separate log functions with a break at about 8 GeV.

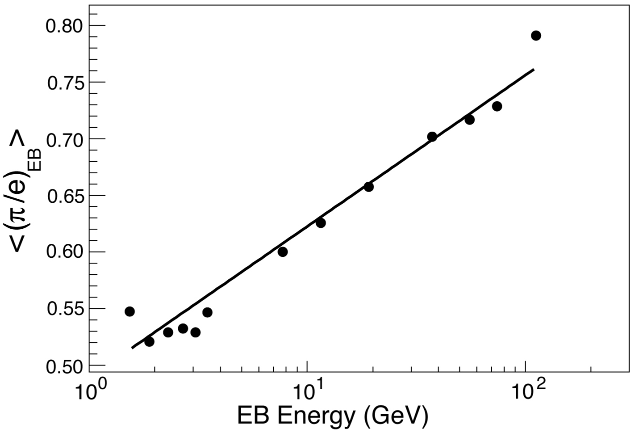

Fig. 18. Measured $(\pi/e)_{\rm EB}$ *vs* $E_{\rm EB}$ after correcting the energies of pions that interacted in the EB (see text for details).

The first task is to parametrize the π/e ratio for the HB and we use events that deposit minimum ionizing energy in the EB ($E_{\rm EB} < 1.2$ GeV). Figure 17 displays the mean of π/e as a function of the measured energy in the HB. The plot (in semi-log) shows two lines with a break point at about 8 GeV. Above $\sim$ 8 GeV, the mean of π/e can be expressed, for example, by a fit using Wigmans' parametrization [15–17] with $e/h = 1.4 \pm 0.1$,

$$< (\pi/e)_{\rm HB} >= \frac{1 + (e/h - 1) \times 0.1 \log(E_{\rm HB})}{e/h} \qquad (1)$$

Below $\sim$8 GeV, π/e is represented by the following logarithmic function

$$< (\pi/e)_{\rm HB} >= 0.179\pm0.005 \log(E_{\rm HB})+0.413\pm0.005. \qquad (2)$$

Another approach is due to Groom [18]: $\pi/e = 1 - (1 - h/e)(E/E_0)^{m-1}$ where E_0 is about 1 GeV and m ranges from 0.80 to 0.85. A fit to the data above 20 GeV without fixing E_0 and m gives the following results: $e/h = 1.5$, $E_0 = 2.5$ GeV and $m = 0.77$. Neither Wigmans nor Groom parametrization works well for the entire energy range from 2 to 300 GeV.

The next step is to correct the energy deposited in the EB using the event-by-event corrected energy values in the HB using Equations 1 and 2. The EB energy is simply the beam energy minus the corrected energy in the HB. The ratio of the computed EB energy divided by the measured energy is π/e (see Equation 3). Since for a particular beam momentum the energy deposited in the EB varies from minimum ionizing to full beam energy, to determine the correction parameters, only the events that deposit significant amount of energy in the HB are selected: $0.2P_b \leq E_{\rm EB} \leq 0.8P_b$, for beam momenta between 4 and 300 GeV/c. For each beam momentum, the average EB energy is computed by using the following formula:

$$\langle(\pi/e)_{\rm EB}\rangle = \frac{\langle E_{\rm EB}\rangle}{P_b - E^*_{\rm HB}} \qquad (3)$$

where $E^*_{\rm HB}$ is the event-by-event corrected HB energy, $E_{\rm HB}/(\pi/e)_{\rm HB}$. In Figure 18 the mean π/e for EB is plotted *vs* the logarithm of the observed mean EB energy. The

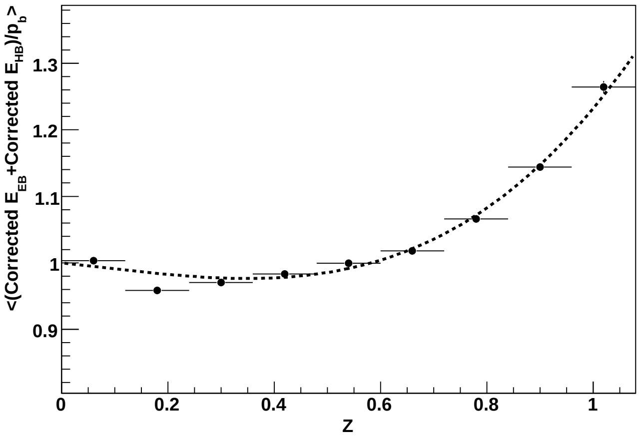

Fig. 19. The π/e corrected response ratio for 100 GeV/c pions of the combined system as a function of the EB fraction. The Z value is defined as $E_{\mathrm{EB}}/(E_{\mathrm{EB}}+E_{\mathrm{HB}})$, ratio of raw energy deposit in the EB with respect to the total in the calorimeter. The smooth curve is a third order polynomial fit to the data (see Eq. 5).

line is fitted to the data with a function of the form

$$\langle(\pi/e)_{\mathrm{EB}}\rangle = a_{\mathrm{E}} \log\left(E_{\mathrm{EB}}\right) + b_{\mathrm{E}}. \tag{4}$$

The best fit parameters are $a_{\mathrm{E}} = 0.057 \pm 0.006$ and $b_{\mathrm{E}} = 0.49 \pm 0.04$.

After correcting the EB energies event-by-event using the above function, $E^{*}_{\mathrm{EB}} = E_{\mathrm{EB}}/(\pi/e)_{\mathrm{EB}}$, we find that the π/e correction overestimates the total EB+HB energy values for events with large EB energy fractions, $Z \equiv E_{\mathrm{EB}}/(E_{\mathrm{EB}}+E_{\mathrm{HB}}) > 70\%$ (see Figure 19). This is expected since these events correspond to the cases when a hadronic shower in the EB fluctuates largely to neutral particles. The final step in the correction parametrization is to linearize the total response of the EB+HB system by fitting the non-linear response to the correction function shown in Figure 19. This set of corrections has been determined to be insensitive to the beam momentum and 100 GeV/c data is a good representation for all other beam momentum data.

$$\left\langle \frac{E^{*}_{\mathrm{EB}} + E^{*}_{\mathrm{HB}}}{P_b} \right\rangle = (0.412 \pm 0.045)Z^3 - (0.096 \pm 0.058)Z^2 - (0.084 \pm 0.018)Z + 1.00 \tag{5}$$

The total response of the EB+HB system can be optimized by applying Equations 1, 2, 4, and 5 event-by-event. These event-by-event corrected EB *vs* HB energy values are shown in Figure 20 for two different beam momenta (20 and 100 GeV/c).

The improvement in the nonlinear behavior and the response with respect to the distributions in Figure 16 is clearly visible in this figure. Figure 21 shows the signal distributions at four beam momenta before and after the corrections. Corrections bring the mean of these distributions to the corresponding beam momentum value.

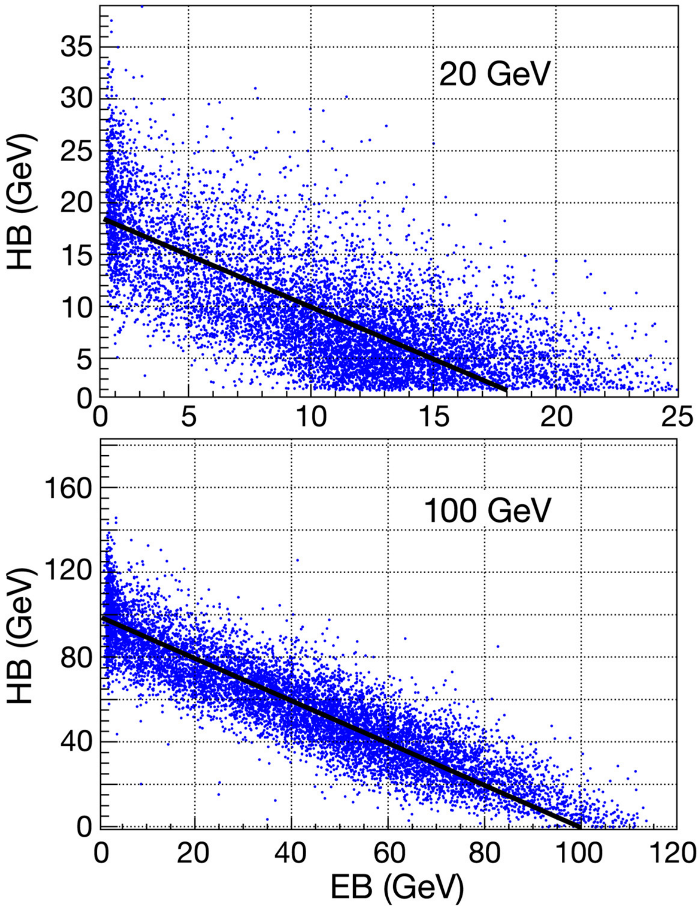

Fig. 20. The EB *vs* HB energy for incident pions of 20 and 100 GeV/c after the two correction methods described in the text are applied.

In order to calculate the energy resolution of the combined EB+HB system, the mean and *rms* values were computed for each momentum. For data of 5 GeV/c and above, a Gaussian fit was also performed for the raw and the corrected data. Below 5 GeV/c, the signal distributions deviate from Gaussian distribution substantially and were not included in the energy resolution determination. Moreover, the correction method did not help improving the response and resolution for 2 and 3 GeV/c data. Figure 22 displays the energy resolution and the response linearity of the combined EB+HB calorimeters for pions. The circles represent the raw and the squares represent the corrected data. Figures 22.a and 22.b are derived from sample means and the *rms* values, whereas Figures 22.c and 22.d are constructed using the Gaussian fit values to the corresponding energy distributions. The energy resolution is customarily parametrized as $\sigma/E = a/\sqrt{E} \oplus b$ where a is the stochastic and b is the constant term, and the terms are added in quadrature. The raw resolution of the EB+HB system is such that $a = 111.5 \pm 2.1\%$ and $b = 8.6 \pm 1.4\%$ as indicated by open black circles within 4 to 300 GeV/c in Figure 22.a. After applying the corrections, the energy resolution improves, $a = 94.3 \pm 1.2\%$

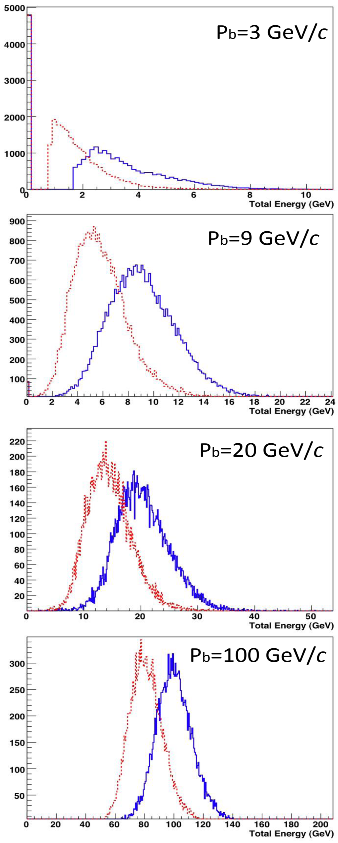

Fig. 21. The signal distributions at four incident π^- beam momenta. The dashed (red) histograms are the raw data and the solid (blue) histograms are after the corrections described in the text.

and $b = 8.4 \pm 1.0\%$ (solid red squares in Figure 22.a.). The open black circles in Figure 22.c display the energy resolution of the combined system when the raw data are fit with a Gaussian distribution at each energy from 5 to 300 GeV/c. This procedure results in $a = 110.7 \pm 3.1\%$ and $b = 7.3 \pm 1.7\%$. The corrections further improve the energy resolution as indicated by the solid red squares in Figure 22.c ($a = 84.7 \pm 1.6\%$ and $b = 7.4 \pm 0.8\%$). The corrected mean response remains constant within 1.3% *rms* as depicted in Figure 22.d.

The method described in this section was developed for improving the total response of the *isolated charged hadron clusters* in the EB+HB. The application of the method (*i.e.*, Equations 1, 2, 4, and 5) requires only the measured cluster energy values in the EB and HB for each event. The method could be further improved by taking into account the transverse energy distribution information in the EB and HB.

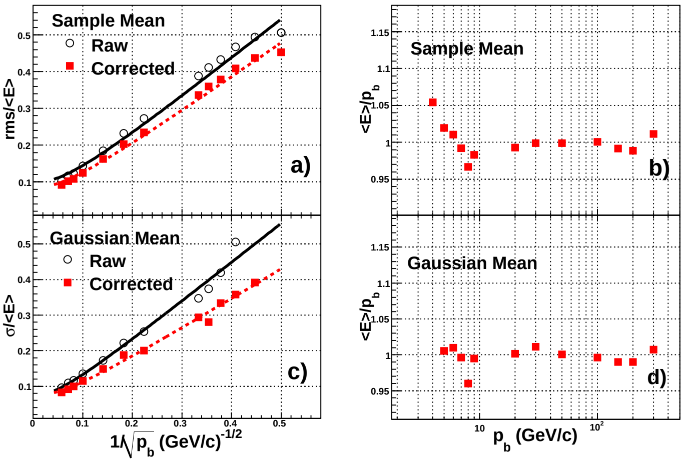

Fig. 22. The energy resolution (a and c) and the corrected response of the combined calorimeters (b and d) before (circles) and after the corrections (squares) are discussed in detail in the text.

6 Summary and Conclusions

The CMS barrel calorimeter has been exposed to particle beams with momenta from 2 to 350 GeV/c. The beam line instrumentation included Cherenkov, time-of-flight, and veto counters, as well as wire chambers. The particle identification was sufficient to separate electrons, muons, pions, kaons and protons of both charges over a substantial energy range. At the higher energies, the CMS outer hadron calorimeter, the HO, was employed to reduce the fluctuations in longitudinal energy leakage.

The response to different hadrons is examined and interesting regularities have emerged. The ratio of negative charged to positive charged pion response, the ratio of negative pion to proton response and the ratio of pions to antiprotons are explored.

Finally, the linearity and energy resolution for negative pions are optimized. The CMS calorimetry is noncompensating and the EB and HB segments are of disparate materials. Thus, the raw response and the energy resolution need to be corrected. In particular, the present data set explores the low energy (below 10 GeV) response where previously used parametrizations no longer fit the data well. Since this is precisely the relevant energy regime for much of the particles in jets, it is important to understand and develop correction strategies.

The π/e ratio of both the EB and HB is fit over $5-300$ GeV/c range. The corrected data are linear within 1.3% (rms) above 5 GeV/c, and the stochastic and the constant energy resolution terms are 84.7±1.6% and 7.4±0.8%, respectively. The calorimeter remains noncompensating, so that a substantial deviation from $E^{-1/2}$ scaling is unavoidable. The applied corrections for pions restore linearity and improve energy resolution. The correction method outlined in this paper is for isolated single particles. The data from these tests however can be applied to jets with the aid of Monte Carlo techniques where the jet response is reconstructed from known individual particles.

7 Acknowledgments

The results presented in this paper are partially based on the doctoral theses of Jordan Damgov [19], Kazim Gümüş [20] and Efe Yazgan [21]. This project was carried out with financial support from CERN, Department of Atomic Energy and Department of Science and Technology of India, U.S. Department of Energy, U.S. National Science Foundation, RMKI-KFKI (Hungary, OTKA grant T 016823), Croatian Ministry of Science, Education and Sport (under grant No. 023-0982887-3064), French CNRS/Institut de Physique Nucleaire et de Physique des Particules, French Commissariat a l'Energie Atomique, Greek General Secretariat for Research and Technology, Italian Istituto Nazionale di Fisica Nucleare, Federal Agency for Science and Innovations of the Ministry for Education and Science of the Russian Federation, Federal Agency for Atomic Energy of the Russian Federation, Russian Academy of Sciences, Ministry of Science of Serbia, Swiss Funding Agencies, Scientific and Technical Research Council of Turkey (TÜBITAK), Turkish Atomic Energy Agency (TAEK), Bogazici University Research Fund (Grant no: 04B301), Science and Technology Facilities Council (UK).

References

1. CMS Collaboration, *The Hadron Calorimeter Project Technical Design Report*, CERN/LHCC 97-31 (1997).
2. CMS Collaboration, *The Electromagnetic Calorimeter Technical Design Report*, CERN/LHCC 97-33 (1997).
3. B. S. Archaya *et al*, The CMS Outer Calorimeter, CMS NOTE-2006/127.
4. S. Abdullin *et al*, Eur. Phys. J. C **53** (2008) 139.
5. S. Abdullin *et al*, Eur. Phys. J. C **55** (2008) 159.
6. V. Abramov *et al*, Nuc. Instr. and Meth. **A457** (2001) 75.
7. G. Baiatian *et al*, Energy Response and Longitudinal Shower Profiles Measured in CMS HCAL and Comparison With Geant4, CMS NOTE-2006/143.
8. G. Baiatian *et al*, Synchronization and Timing in CMS HCAL, CMS NOTE-2006/139.
9. W. Bertl *et al*, Eur. Phys. J. C **41**, s02 (2005) 11.
10. P. Adzic *et al*, Eur. Phys. J. C **44**, s02 (2006) 1.
11. Freon134a is an ozone-friendly gas. Based on the measurements during the beam test, we find Freon 134a's refractive index to be 1.00065, which is also consistent with the estimates based on its molecular weight.
12. M. Adams *et al*, Nucl. Instr. and Meth. **A511** (2003) 311.
13. C. Amsler *et al*, Physics Letters **B667** (2008) 1.
14. N. Akchurin *et al*, Nucl. Instr. and Meth. **A408** (1998) 380.
15. The ratio of conversion efficiencies of the electromagnetic and hadronic energy depositions to electrical signals is called the intrinsic e/h ratio. The ratio of responses to incident pions to incident electrons at a given energy is related to e/h as "π/e" $= [1 + (e/h - 1)f_0]/(e/h)$ where the electromagnetic fraction $f_0 = 0.1 \log P_b$ and P_b is the beam momentum.
16. R. Wigmans, Nucl. Instr. and Meth. **A265** (1988) 273.
17. C. W. Fabjan and T. Ludlam, Ann. Rev. Nucl. Part. Sci. **32** (1982) 335.
18. T. A. Gabriel *et al*, Nucl. Instr. and Meth. **A338** (1994) 336.
19. J. Damgov, Ph.D. thesis, Institute for Nuclear Research and Nuclear Energy, Bulgarian Academy of Science, Sofia, Bulgaria (unpublished), 2008.
20. K. Gümüş, Ph.D. thesis, Texas Tech University, CERN-THESIS-2008-066.
21. E. Yazgan, Ph.D. thesis, Middle East Technical University, Ankara, Turkey, Fermilab-thesis-2007-13.